ACS NANO
www.acsnano.org

In Situ Surface Reconstruction via Lithium Residue Regulation for Direct Recycling of Ni-Rich Cathodes

Jiao Lin, Varun Gupta, Xiaolu Yu, Yuwei Zhu, Dong Ju Lee, Zishuo Zhao, Xianghui Xiao, Greta Feagure, Feng Li, Hongpeng Gao, Dennis Nordlund, Linqin Mu,* and Zheng Chen*

Cite This: https://doi.org/10.1021/acsnano.5c13656 Read Online

ACCESS | Metrics & More | Article Recommendations | Supporting Information

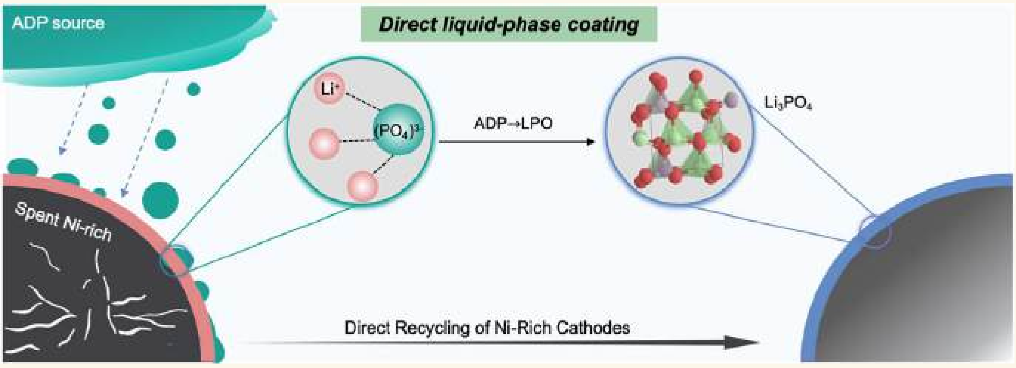

ABSTRACT: **Surface stability is crucial for the long cycling performance of Ni-rich cathodes, as it dictates and governs side reactions, preserves crystal integrity, and mitigates capacity degradation during cycling. For spent Ni-rich cathodes targeted for one-step direct recycling, constructing a robust and stable surface is particularly challenging because prior cycling induces severe structural and morphological degradation. Here, we introduce an in situ surface reconstruction strategy that converts surface lithium residues into a protective layer via a direct liquid-phase coating with ammonium dihydrogen phosphate (ADP). During the process, residual lithium remaining after the hydrothermal relithiation is removed, while a conformal lithium phosphate (Li_3PO_4, LPO) layer is formed to act as both a chemical barrier and a structural stabilizer. This dual function enhances cycling stability and rate capability in regenerated cathodes, and the approach is applicable to various Ni-rich compositions including spent $LiNi_{0.6}Co_{0.2}Mn_{0.2}O_2$ (NCM622) and scrap $LiNi_{0.866}Mn_{0.066}Co_{0.05}Al_{0.018}O_2$ (NCMA). Its scalability and compositional versatility make it a promising route for sustainable regeneration of high-performance cathode materials.**

KEYWORDS: *spent lithium-ion batteries, Ni-rich cathodes, in situ surface reconstruction, direct recycling, lithium phosphate layer*

The accelerating transition toward renewable energy systems and electric mobility has intensified the global demand for high-energy-density lithium-ion batteries (LIBs).[1] Among various cathode chemistries, nickel (Ni)-rich layered oxides, such as $LiNi_xCo_yMn_{1-x-y}O_2$ ($0 < x, y < 1, x \geq 0.6$, NCM) and $LiNi_xCo_yMn_zAl_{1-x-y-z}O_2$ ($0 < x, y, z < 1, x \geq 0.85$, NCMA), are among the most promising candidates owing to their high specific capacity and energy density.[2] Despite their promise, these materials face major bottlenecks that limit their commercial viability. Structural instability, interfacial degradation, and accelerated capacity fading during cycling remain persistent challenges for high-Ni compositions.[3] These issues are further amplified in end-of-life cathodes, where phase impurities, surface deconstruction, and residual lithium compounds hinder both performance and recyclability.[4] Recycling Ni-rich cathodes not only offsets the environmental and economic costs associated with primary resource extraction but also contributes directly to climate and

Received: August 11, 2025
Revised: November 12, 2025
Accepted: November 13, 2025

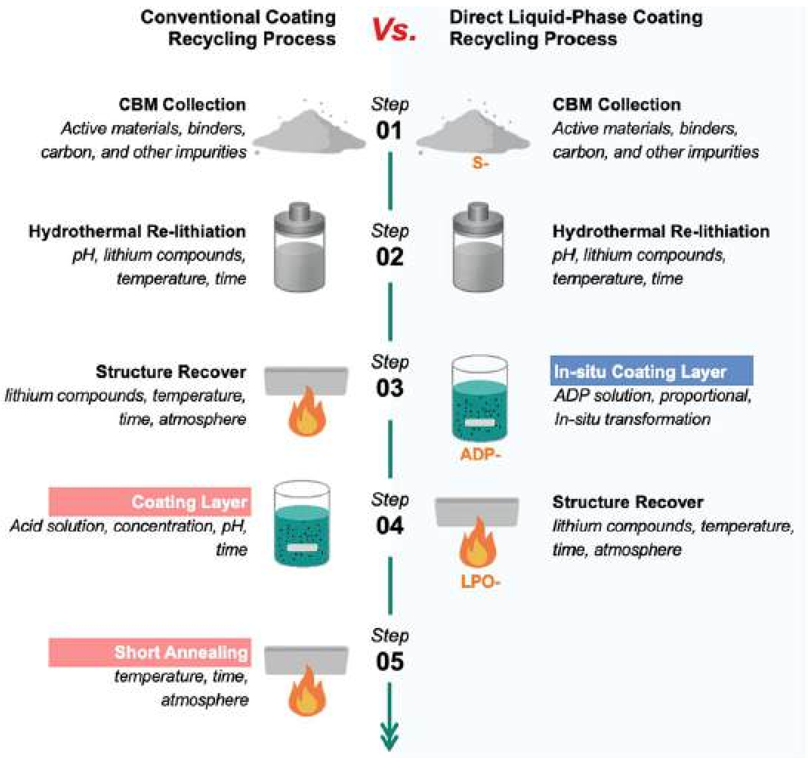

Figure 1. Schematic illustration of the in situ surface reconstruction method. The diagram compares the in situ surface reconstruction approach enabled by lithium residue regulation in Ni-rich particles with the conventional coating recycling process, which typically requires short-annealing at ∼500 °C for several hours.

sustainability goals. Therefore, addressing the degradation issues is imperative for closing the loop on battery materials and advancing circular energy storage technologies.

Conventional recycling approaches, including pyrometallurgical and hydrometallurgical processes, are energy-intensive and often result in significant material losses.[5] These methods are also ill-suited for preserving the delicate crystal structures of Ni-rich cathodes, thereby limiting their ability to restore high-performance materials. In contrast, direct recycling, particularly hydrothermal relithiation coupled with moderate annealing, has gained traction for its ability to preserve crystallinity and restore electrochemical function across a range of chemistries, including $LiCoO_2$ (LCO),[6] $LiMn_2O_4$ (LMO),[7] NCM,[8] and $LiFePO_4$ (LFP).[9] Our previous work demonstrated a scalable regeneration pathway for spent NCM111 via purification and relithiation of cathode black mass (CBM), achieving production at the 100 g batch scale.[10] Despite these advances, residual surface impurities and interfacial degradation remain persistent barriers in relithiated cathodes, especially those with high Ni content.[11] Residual lithium compounds (mainly LiOH and Li_2CO_3 after relithiation) on the cathode surface can trigger parasitic reactions, induce phase transformations, and accelerate structural degradation, ultimately compromising battery stability and safety. This issue is particularly critical for high-Ni cathodes, where the tendency to form residual lithium species during regeneration leads to surface instability. Overcoming such challenges requires integrated approaches that not only restore the bulk composition but also repair surface damage and stabilize the electrode−electrolyte interface.

Surface engineering has proven essential for enhancing cathode durability by passivating the electrode−electrolyte interface and mitigating degradation pathways.[12] Advanced coating strategies, ranging from ceramic to polymeric and composite layers, have shown efficacy in reducing side reactions, suppressing phase transitions, and stabilizing surface structures.[13] However, these conventional approaches often involve in multistep, postsynthesis modifications such as coating precursor preparation, high-temperature annealing, or sequential deposition.[14] These processes not only increase processing complexity and cost but may also induce further surface damage or composition mismatch, particularly during repeated heating cycles.[15] Such limitations restrict the scalability and sustainability of current coating technologies, particularly for large-scale recycling applications. Furthermore, most coating techniques focus on post-treatment modifications, which fail to address the root cause of surface degradation: the residual lithium species formed during direct recycling processes. Effectively regulating these residues is critical for maintaining the integrity of the regenerated cathode and preventing surface-related performance losses.

To address these limitations, we report a direct aqueous-phase surface engineering strategy that simultaneously removes lithium residues and forms a conformal Li_3PO_4 (LPO) coating on spent Ni-rich cathodes. The novelty of this approach lies in the integration of lithium residue regulation with the formation of a stable, protective surface layer without going through a separate solution process, which is commonly used in the literature[16] and practical manufacturing.[17] This dual functionality mitigates surface oxidation, prevents the dissolution of transition metals, and enhances the stability of the electrode−electrolyte interface. We demonstrate the broad applicability of this method using two representative Ni-rich cathodes, spent $LiNi_{0.6}Co_{0.2}Mn_{0.2}O_2$ (NCM622) and scrap Li-

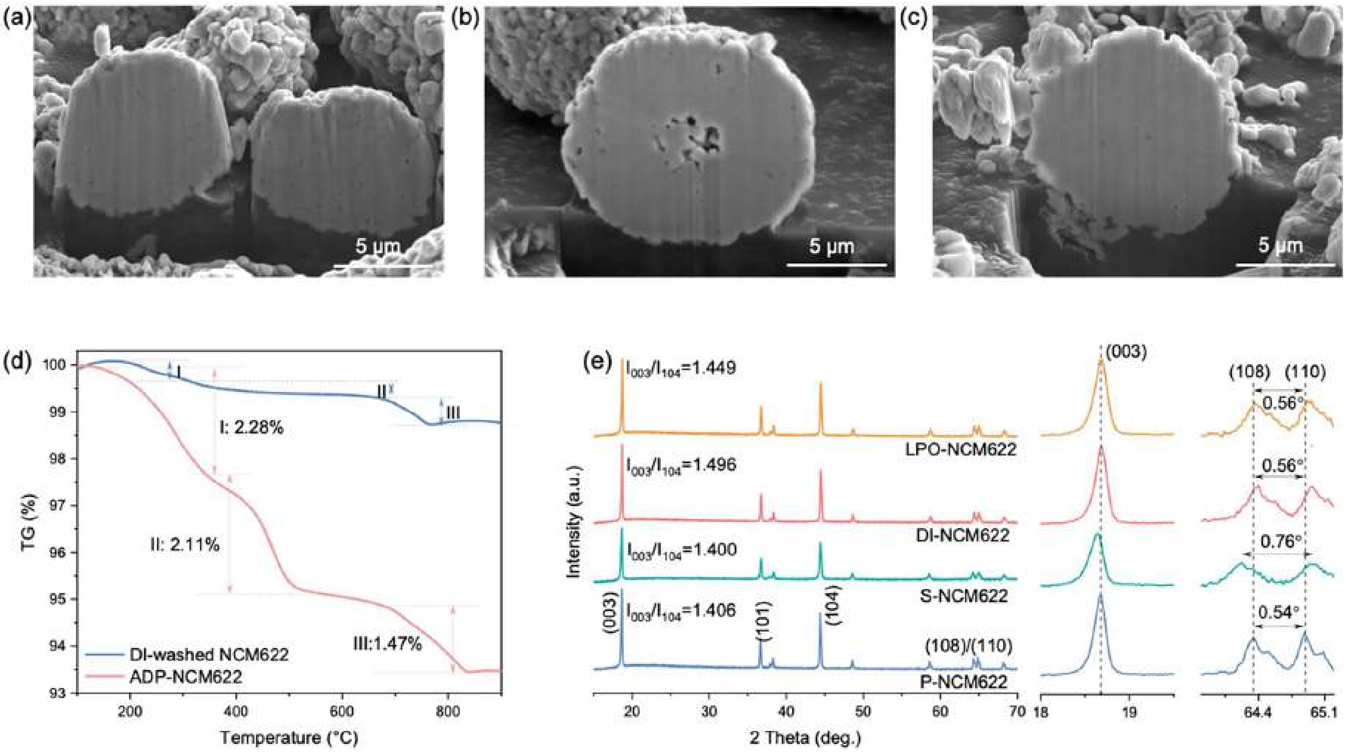

Figure 2. Surface and bulk structural evolution, phase transformation, and thermodynamic analysis of NCM622 during the in situ surface reconstruction process. Cross-sectional SEM images of (a) P-NCM622, (b) S-NCM622, and (c) LPO-NCM622 particles. (d) TGA profiles of ADP- NCM622 (1 wt % ADP) and DI-washed NCM622 powders, both mixed with an additional 5 mol % Li_2CO_3. (e) XRD patterns of various NCM622 samples.

$Ni_{0.866}Mn_{0.066}Co_{0.05}Al_{0.018}O_2$ (NCMA), which differ in composition and surface reactivity. The resulting LPO-coated materials exhibit improved cycling stability, rate performance, and surface integrity compared with pristine samples. Additionally, the process is environmentally benign, leveraging an aqueous-based process that aligns with green chemistry principles. The method is compatible with existing recycling workflows, making it operationally scalable and industrially viable. By combining surface reconstruction and lithium residue regulation into a single green processing step, this strategy addresses a critical gap in cathode regeneration, offering a scalable and sustainable pathway for next-generation LIB recycling.

RESULTS AND DISCUSSION

Surface Reconstruction by Residual Lithium Conversion. In a typical hydrothermal direct recycling process, the separated CBM powder is treated in an aqueous LiOH solution under an elevated temperature (100−220 °C) and pressure. This treatment facilitates lithium insertion, structural restoration, and impurity removal.[10,18,19] Following the hydrothermal relithiation and subsequent separation, residual lithium often remains on the surface of Ni-rich cathodes, leading to interfacial instability and degradation during later battery cycling.[10] To simultaneously address this issue and repair the inherent structural defects, we developed a solution-mediated surface reconstruction strategy that leverages the spontaneous precipitation of Li_3PO_4 in aqueous environments, a material well-known for its high Li^+ conductivity and widespread applications as a coating on Ni-rich layered cathodes.[20] In this context, the presence of residual Li^+ and phosphate ions (PO_4^{3-}) facilitates the formation of Li_3PO_4 via a straightforward acid−base reaction ($3Li^+ + PO_4^{3-} \rightarrow Li_3PO_4$), analogous to coprecipitation mechanisms commonly used in wet-chemical synthesis.[21] Leveraging this chemistry, we developed an in situ surface reconstruction strategy that capitalizes on solution-mediated phase formation under mild conditions (Figure S1), enabling effective surface modification without the need for further high-temperature processing. Specifically, hydrothermal relithiated Ni-rich cathodes were briefly rinsed with deionized (DI) water to separate the NCMs from the Li-containing solution and then immersed in an aqueous solution of ammonium dihydrogen phosphate (ADP). This treatment enabled the in situ formation of a conformal phosphate layer on NCM particles (ADP-NCM), which was subsequently crystallized through a brief annealing step to yield the surface-reconstructed Li_3PO_4-coated NCM material (LPO-NCM).

The overall process is illustrated in Figure 1, alongside a conventional ex situ coating strategy employed in today's recycling workflows, which typically requires extended high-temperature annealing following relithiation to recover the bulk crystal structure.[22] To evaluate the efficacy of this method, spent NCM622 (S-NCM622) was first employed as a representative model system, while pristine NCM622 (P-NCM622) served as the reference. We first confirmed that this method can introduce phosphate species on NMC622 particles (i.e., ADP- and LPO-treated samples) through scanning electron microscopy (SEM) and energy-dispersive spectroscopy (EDS) analyses (Figures S2−S7). Notably, cross-sectional SEM images (Figure 2a−c) demonstrate that the direct liquid-phase coating recycling process approach effectively preserves the microstructure of NMC622, characterized by well-

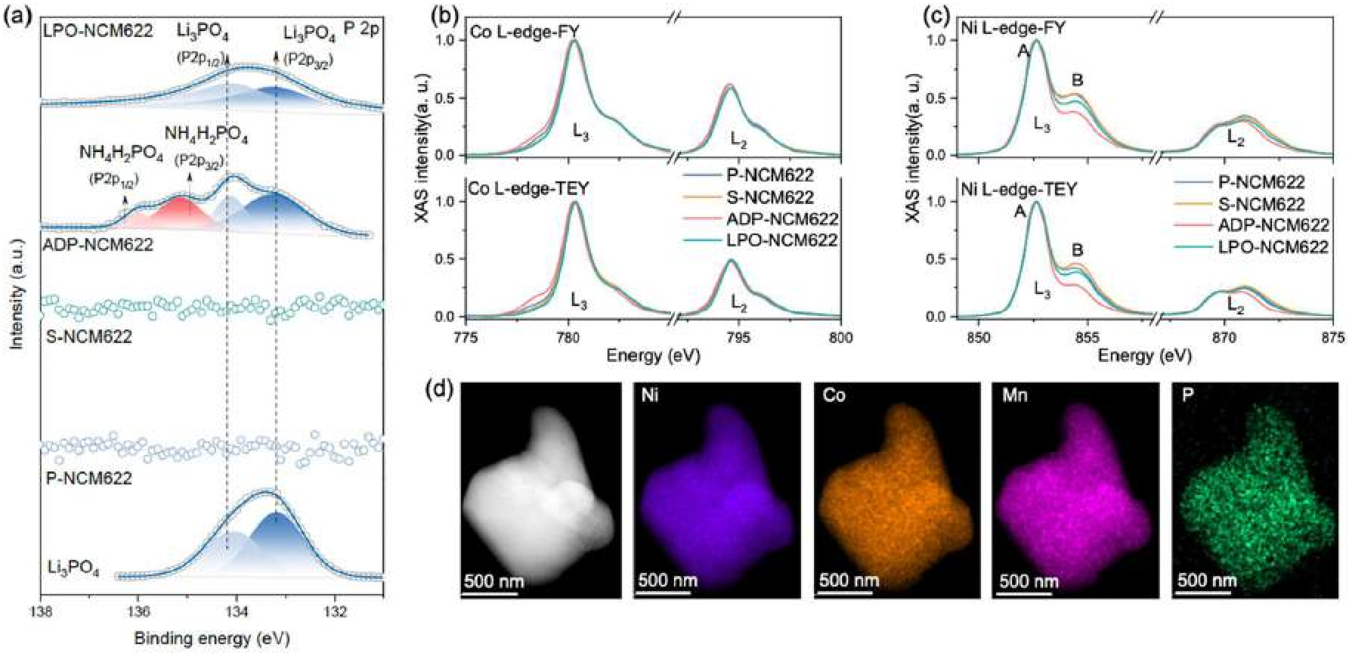

Figure 3. Phase determination and valence uniformity analyses of the in situ surface reconstruction process. (a) ADP-LPO evolution during the in situ surface reconstruction and LPO coating is characterized by analyzing P 2*p* spectra of different NCM622 powders, with standard Li_3PO_4 included for comparison. (b) Ni *L*-edge and (c) Co *L*-edge XAS spectra of various NCM622 powders, collected in both TEY and FY modes. (d) TEM image and corresponding EDS elemental mapping of a LPO-NCM622 particle.

maintained grain boundaries and a marked reduction in void formation compared to the degraded spent material.

To further understand the phosphate coating layer, we conducted thermogravimetric analysis (TGA) to elucidate its behavior by analyzing the thermal events occurring during the annealing process (Figure 2d). The DI-washed sample exhibited a minor weight loss upon heating, attributed primarily to the dehydration of residual LiOH and the decomposition of LiOH and Li_2CO_3. In contrast, the ADP-NCM622 sample displayed three distinct weight-loss events attributed to (i) the dehydration of residual LiOH and $NH_4H_2PO_4$,[23] (ii) the acid−base reaction between LiOH and H_3PO_4 forming Li_3PO_4,[24] and (iii) the fusion of lithium oxide (Li_2O),[25] as summarized in Table S1. These results confirm that the entire liquid-phase coating process not only removes lithium residues but also drives the in situ formation of a stable phosphate coating during heating. Powder X-ray diffraction (XRD) and inductively coupled plasma mass spectrometry (ICP-MS) were employed to assess the structural integrity and lithium content across samples (Figure 2e and Table S2). All samples retain the α-$NaFeO_2$ layered structure with $R\bar{3}m$ symmetry, confirming the absence of bulk phase transitions during regeneration.[26] The (003) reflection in S-NCM622 shifts to a higher 2θ, indicating expansion of the *c*-lattice parameter due to lithium deficiency and enhanced electrostatic repulsion between oxygen planes.[27] This shift is fully reversed in DI-NCM622 and LPO-NCM622, suggesting a successful lithium replenishment. Furthermore, the intensity ratio of the (003)/(104) peaks, a proxy for cation disorder, improves from 1.40 in S-NCM622 to 1.45 in LPO-NCM622, indicating reduced cation mixing and improved layered ordering.[28] The narrowed (108)/(110) doublet spacing in regenerated samples further supports the recovery of the original Ni valence state and the lattice symmetry.

To investigate surface reconstruction and chemical evolution during the regeneration process, we employed X-ray photoelectron spectroscopy (XPS) and soft X-ray absorption spectroscopy (XAS) on a series of NCM622 cathodes. The P 2*p* XPS spectrum of ADP-NCM622 reveals mixed phosphate species, including residual ADP and partially formed Li_3PO_4 (Figure 3a). After annealing, the LPO-NCM622 spectrum exhibits a single P 2*p* signal consistent with Li_3PO_4 phase formation, confirming complete surface conversion. XAS spectra at the Co, Ni, and Mn *L*-edges provide a depth-sensitive insight into redox chemistry. Co *L*-edge spectra in both total electron yield (TEY, ∼5 nm depth) and fluorescence yield (FY, ∼50−100 nm) modes are nearly identical (Figure 3b), indicating a uniform Co^{3+} oxidation state across the surface and bulk.[29] In contrast, Ni *L*-edge spectra (Figure 3c) display distinct multiplet features at the L_3-edge (peaks A and B), where the B/A intensity ratio correlates with the oxidation state.[30,31] Across samples, the B/A ratios in the Ni *L*-edge FY mode are slightly higher than those in the TEY mode, indicating a reduced Ni oxidation state at the particle surface compared to bulk, consistent with intrinsic surface instability.[3] In S-NCM622, this discrepancy disappeared, suggesting uniform Ni^{3+} formation due to a lithium deficiency. ADP treatment partially suppresses Ni oxidation for both surface and bulk, likely due to the passivating effect of phosphate adsorption. LPO-NCM622 shows restored but slightly lower Ni oxidation than pristine, possibly due to phosphate stabilization. The Li_3PO_4 layer acts as a chemically stable lithium-containing phase at the particle surface. It provides a local lithium reservoir that helps maintain a moderate chemical potential for lithium at the surface, thereby stabilizing Ni in a slightly lower oxidation state without further delithiation or cation migration.[32]

Mn *L*-edge spectra were collected in the TEY mode to avoid distortions caused by self-absorption and saturation effects in

https://doi.org/10.1021/acsnano.5c13656
ACS Nano XXXX, XXX, XXX−XXX

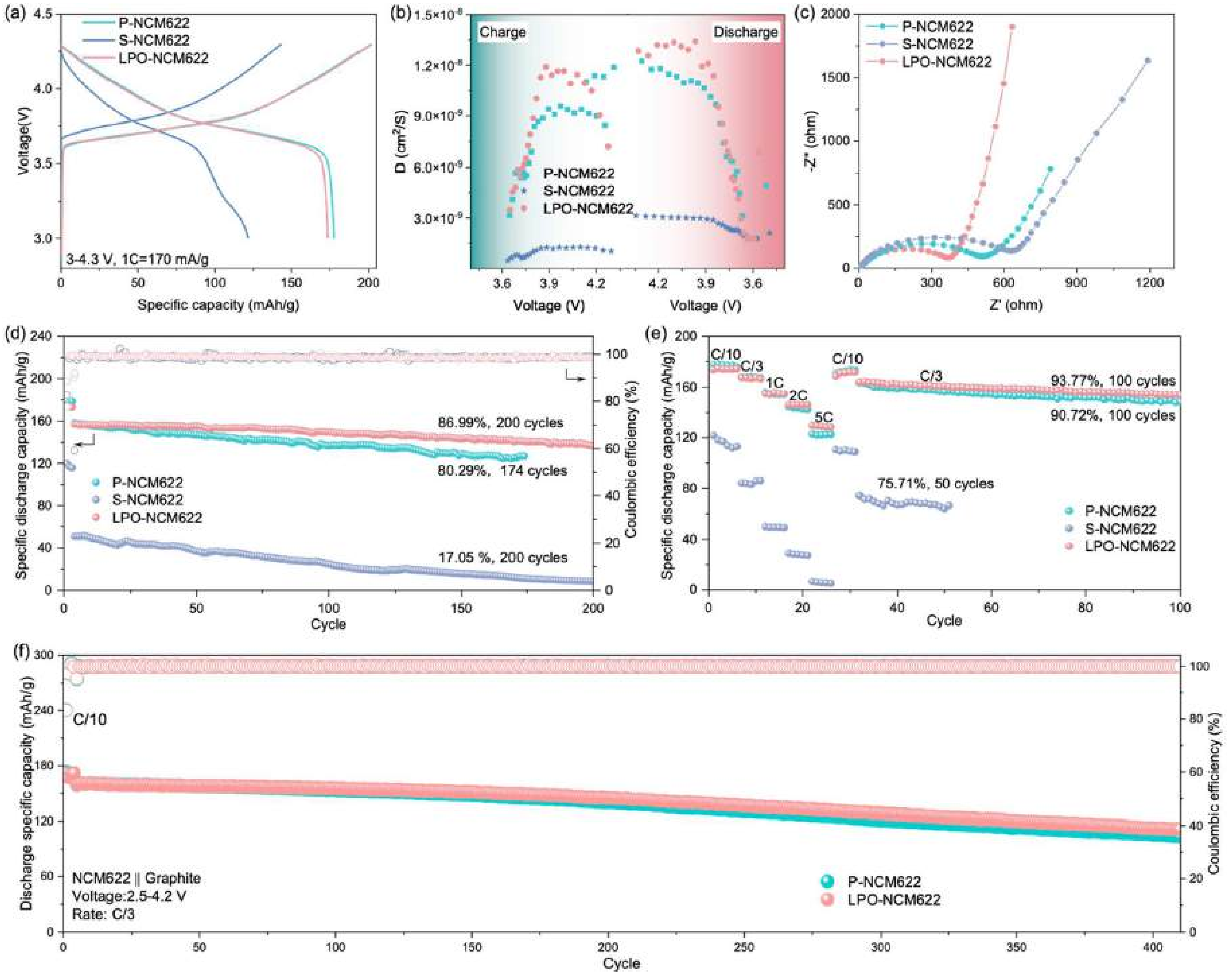

Figure 4. Electrochemical performance of the cells containing S-NCM622, P-NCM622, and LPO-NCM622 with 1 wt % ADP materials. (a) Initial charge–discharge profiles at C/10. (b) Li^+ diffusion coefficients calculated from GITT measurements. (c) Impedance spectra profile of different NCM622 electrodes in coin-type cells before cycling. (d) Cycling performance at C/3 and (e) rate capability comparison in coin-type half cells. (f) Full-cell cycling stability of LPO-NCM622 compared to the P-NCM622 at C/3.

FY.[33] S-NCM622 showed Mn^{2+} signals from surface reduction and Mn dissolution, while P-, ADP-, and LPO-NCM622 samples exhibited Mn^{4+} features (Figure S8), consistent with full oxidation state restoration.[34,35] Transmission electron microscopy (TEM) further confirms a uniform phosphorus-rich layer surrounding NCM622 particles, supporting the presence of a conformal Li_3PO_4 coating of 2−5 nm (Figures 3d and S9). Together, these results demonstrate that the aqueous-phase phosphate treatment not only removes residual lithium but also induces the controlled precipitation of a protective, chemically stable Li_3PO_4 layer. Collectively, these findings establish that our aqueous-phase ADP treatment achieves both chemical and structural regeneration of Ni-rich cathodes. The in situ Li_3PO_4 coating restores oxidation state homogeneity across Co, Ni, and Mn and reinforces interfacial stability.

Electrochemical Performance of Surface-Reconstructed Cathodes. To determine the optimal conditions for in situ surface reconstruction, we systematically evaluated the effect of the ADP ratio on structural characteristics and electrochemical performance of regenerated Ni-rich cathodes. The titration results show a progressive increase in titratable Li content as the ADP ratio increased from 0.5 to 2 wt % (Table S3). This trend is attributed to the formation and surface accumulation of Li_3PO_4, which remains detectable during titration under acidic conditions. Upon subsequent calcination, the surface Li content significantly decreased across all samples (LPO−). The sample treated with 0.5 wt % ADP retained slightly more lithium, while the difference among the other three samples was marginal, suggesting that 1 wt % ADP is sufficient to consume the surface lithium species. Additionally, XRD analysis shows that all samples preserve the layered $R\bar{3}m$ phase, and varying the ADP concentration from 0.5 to 2 wt % induces no significant changes to the bulk crystal structure (Figure S10), confirming that phosphate treatment does not disrupt the layered $R\bar{3}m$ phase. However, electrochemical measurement revealed a strong dependence of the performance on the ADP content. Among all conditions, LPO-NCM622 that was prepared with 1 wt % ADP exhibited the best rate capability, whereas annealing alone restored the initial discharge of NCM622 but failed to recover its rate capability (Figure S11). This performance optimization can be attributed to a balance between surface protection and Li^+ transport,

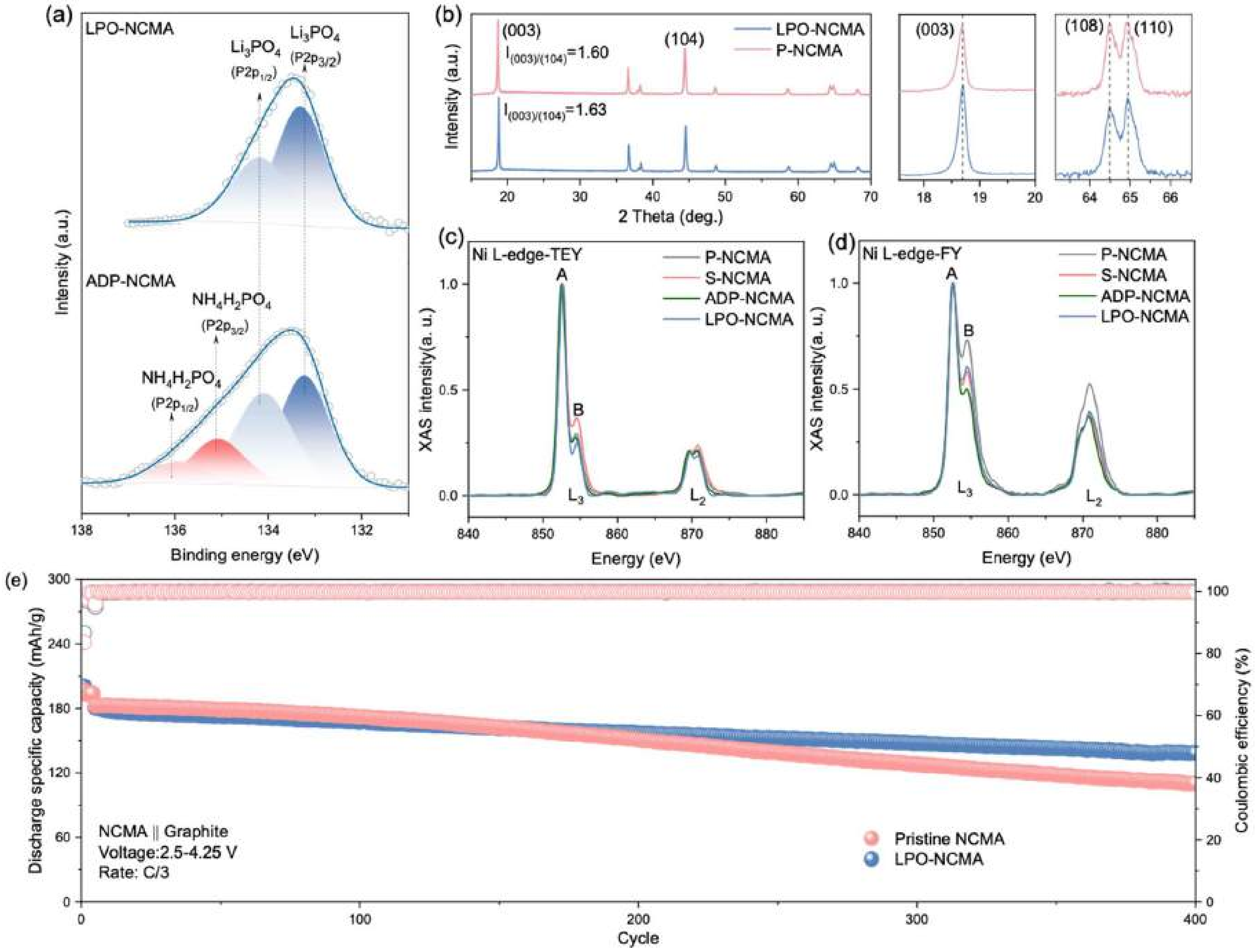

Figure 5. Universality and scale-up validation of the in situ surface modification strategy applied to NCMA chemistry. (a) ADP-LPO evolution during the in situ surface modification and LPO coating by analyzing P 2*p* spectra of P- and LPO-NCMA samples. (b) XRD patterns of P-NCMA and LPO-NCMA samples. Soft XAS spectra of various NCMA powders at the Ni *L*-edge collected in (c) TEY mode and (d) FY mode. (e) Full-cell cycling performance of LPO-NCMA compared to P-NCMA at C/3.

ensuring both interfacial stability and efficient ion mobility. At low ADP concentrations (<1 wt %), the phosphate coverage on each particle may be incomplete, potentially leaving a portion of the particle surface exposed and susceptible to degradation pathways such as transition metal dissolution and the formation of resistive surface phases. These processes could contribute to reduced capacity retention and structural stability. In contrast, excessive ADP (>1 wt %) may result in a thick Li_3PO_4 coating that, while protective, could hinder Li^+ diffusion across the electrode−electrolyte interface, impairing cycling performance. The 1 wt % ADP content appears to offer a balance, producing a uniform, conformal Li_3PO_4 layer that may provide effective surface passivation while maintaining favorable ion transport kinetics.

Figure 4a shows the initial charge/discharge profiles of the various NCM622 cathodes in coin-type half cells. All samples exhibit similar voltage profiles yet show notable differences in capacity and initial Coulombic efficiency (ICE, Table S4). S-NCM622 delivered the lowest discharge capacity of 121.8 mA h g^{-1} with an ICE of 84.9%. In comparison, P-NCM622 achieved 177.8 mA h g^{-1}, while LPO-NCM622 delivered a discharge capacity comparable to that of an improved ICE of ∼88.6%, indicating partial restoration of the electrochemical integrity. To compare Li^+ transport behavior, a galvanostatic intermittent titration technique (GITT) and electrochemical impedance spectroscopy (EIS) were conducted. As shown in Figure 4b, the apparent Li^+ diffusion coefficients of LPO-NCM622 closely match those of P-NCM622 throughout most of the voltage range. At the same time, S-NCM622 exhibits significantly slower diffusion, reflecting hindered transport through degraded surfaces. This was further corroborated by EIS (Figure 4c), where S-NCM622 displayed a much larger semicircle in the high-to-medium frequency range, indicating elevated charge-transfer resistance. In contrast, LPO-NCM622 exhibited significantly lower resistance, suggesting enhanced surface conductivity and interfacial stability because of the phosphate coating.

Long-term cycling tests further validated the effectiveness of this regeneration strategy. LPO-NCM622 maintained the highest capacity retention of 87.0% after 200 cycles at C/3 at room temperature, outperforming P-NCM622, which retained 80.3% after 174 cycles (Figure 4d, statistical data in Figure S12a). In rate performance tests (Figure 4e; statistics provided in Figure S12b), LPO-NCM622 matched the behavior of the pristine material across a range of current densities, while S-NCM622 showed substantially reduced

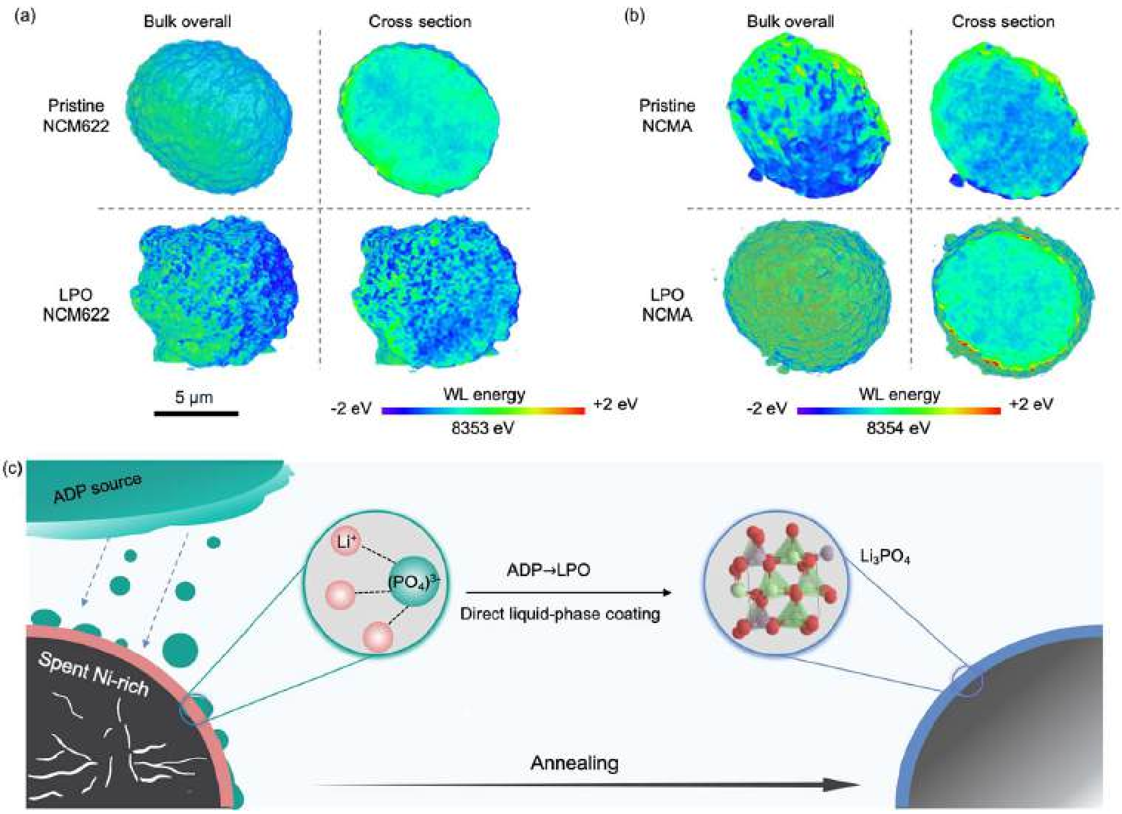

Figure 6. Surface redox heterogeneity and mechanism illustration of the in situ surface reconstruction process. 3D Ni K-edge white-line energy maps of (a) P-NCM622 and LPO-NCM622 particles and (b) P-NCMA and LPO-NCMA particles, revealing surface redox state evolution upon ADP-derived Li_3PO_4 coating. The energy bar for LPO-NCM622 is centered, while the left one corresponds to P-NCM622, P-, and LPO-NCMA. Overall energy distribution histograms of (c) P-NCM622, (d) LPO-NCM622, and (e) P- and LPO-NCMA particles. (f) Schematic illustration of the in situ surface reconstruction mechanism via Li_3PO_4 formation.

capacity at higher rates. To evaluate the practical applicability, full cells were assembled using LPO-NCM622 cathodes and graphite. These cells delivered initial capacities equivalent to those with pristine cathodes and demonstrated a superior cycling stability (Figure 4f), highlighting the translational potential of the regeneration strategy. Together, these results indicate that the optimized ADP-mediated surface reconstruction, particularly with 1 wt % loading, enables the formation of a conformal Li_3PO_4 layer that not only passivates the degraded surface but also facilitates efficient lithium-ion transport.

Universality and Scale-up Verification. To further validate the generality and scalability of our surface reconstruction strategy, we applied the same aqueous-phase phosphate treatment to industrial NCMA cathodes. Notably, these as-received NCMA materials contained poly(vinylidene fluoride) (PVDF) binders and conductive carbon, simulating realistic recycling feedstocks. XPS confirmed that the surface chemical evolution in scrap NCMA followed the same trend as observed in NCM622: the ADP-treated surface exhibited mixed phosphate species, which are fully converted to Li_3PO_4 upon annealing (Figure 5a). XRD analysis reveals complete recovery of the layered $R\bar{3}m$ phase, with the (003) reflection realigned to its pristine position and the spacing of the (108)/(110) doublet restored (Figure 5b), indicative of preserved structural integrity. The (003) to (104) peak intensity ratio increased after treatment, suggesting reduced cation mixing and improved structural ordering. ICP-MS (Table S5) confirms compositional recovery. These results indicate the effective lithium replenishment and restoration of lattice parameters. The soft XAS spectra of the Ni and Co L-edges (Figures 5c,d and S13) show minimal changes in average oxidation states after treatment from the surface to the bulk. Notably, the Ni oxidation state at the surface is lower than that in the bulk, indicating that the liquid-phase phosphate coating primarily affects the surface and does not perturb the bulk redox environment, thereby preserving the intrinsic electrochemical characteristics of the NCMA lattice.

Electrochemical testing further validated the effectiveness of the approach. The LPO-NCMA cathode exhibited an initial discharge capacity of 199.9 mA h g^{-1}, only ~2.5% lower than the pristine counterpart (204.9 mA h g^{-1}) (Figure S14). The slightly reduced capacity is attributed to a suppressed H_2-H_3 phase transition, as revealed by differential capacity (dQ/dV) analysis (Figure S15). Importantly, this suppression correlates with enhanced cycling stability (Figure S16), as the LPO layer mitigates interfacial stress and structural collapse during deep delithiation.[13] To demonstrate process scalability, we applied the same treatment to a 70 g batch of scrap NCMA (Figure S17). The resulting LPO-NCMA powder retained a uniform morphology (Figure S18). Full coin-cell tests reveal excellent long-term cycling performance, outperforming pristine NCMA in terms of capacity retention (Figure 5e). These results highlight the robustness, versatility, and industrial relevance of the developed surface reconstruction strategy.

Mechanism of the Direct Liquid-Phase Coating Recycling Process. To quantify the effects of phosphate-based surface reconstruction, we conducted 3D transmission X-ray microscopy (TXM) coupled with X-ray near energy absorption spectroscopy (XNEAS) at the Ni K-edge on both pristine and phosphate-coated NCM622 and NCMA particles. This technique provides a spatial resolution of ∼30 nm, allowing us to understand the oxidation state distribution of transition metals within a single particle. The 3D white-line energy maps offer a comparative view of the surface and bulk redox states for both NCM622 and NCMA cathodes, before and after surface reconstruction (Figure 6a,b).

The pristine NCM622 particle exhibits a well-balanced Ni^{2+}/Ni^{3+} ratio with minimal surface oxidation indicated by the uniform blue-green distribution (Figure 6a). This stable redox profile suggests that pristine NCM622 inherently possesses chemical uniformity across both the surface and bulk regions. The absence of localized red regions reflects the inherent stability of the material and its resistance to surface degradation. To quantitatively evaluate changes in the redox environment, energy distribution histograms were generated from the 3D TXM data. The histogram exhibits a narrow, symmetric peak centered around 8353.6 eV (Figure S19a), indicating a stable and homogeneous oxidation state with minimal surface degradation. This narrow distribution confirms the uniform redox state of pristine NCM622 and correlates well with the consistent blue-green coloration seen in the 3D map. After ADP treatment and thermal annealing, the LPO-NCM622 sample displays a deeper blue coloration on the energy map, indicating a reduction of Ni^{3+} to Ni^{2+}. This is further confirmed by the lower white-line energy (∼8532.5 eV) observed in the histogram (Figure S19b). The broadened energy distribution suggests that while the Li_3PO_4 coating effectively reduces surface Ni^{3+}, it also introduces slight heterogeneity, likely due to variable coating thickness. Despite this minor heterogeneity, the overall reduction in the white-line energy indicates that the phosphate coating effectively stabilizes the surface, thereby enhancing long-term interfacial integrity.

In contrast, pristine NCMA displays significant red patches, especially near the particle edges, indicating surface heterogeneity and localized oxidation (Figure 6b). This sample has been stored for certain in a glovebox after General Motors (GM) sent it from their facility; the uneven Ni oxidation likely arises from surface defects or reconstruction that developed during storage. Such spatially heterogeneous redox states reflect the intrinsically unstable nature of Ni-rich materials, which are prone to surface degradation, even under inert conditions. The heterogeneous redox states are consistent with the tendency of high-Ni compositions to develop oxidized surfaces due to Ni^{3+} enrichment. This behavior underscores the high surface reactivity and structural instability characteristic of NCMA. The histogram exhibits a sharp, asymmetric peak at ∼8353.5 eV (Figure S17c), reflecting surface oxidation heterogeneity and a high Ni^{3+} content. This instability is consistent with the significant surface degradation typically observed in Ni-rich cathodes, especially after extended cycling. The asymmetry of the peak further highlights the nonuniform distribution of oxidation states, suggesting a mixture of Ni^{2+} and Ni^{3+} species at the surface.

After phosphate surface reconstruction, the LPO-NCMA sample shows a more uniform blue-green profile on the 3D map, indicating reduced surface oxidation and improved redox uniformity. The histogram for LPO-NCMA shows a slightly broader and shifted lower white-line energy peak at ∼8353.2 eV (Figure S17c), along with a more homogeneous color distribution (blue-green to light green) compared to P-NCMA. This shift indicates a partial reduction of Ni^{3+} to Ni^{2+} while maintaining localized redox stability. This redox adjustment suggests that the LPO coating primarily acts as a protective layer, maintaining the Ni dominance while modulating localized redox variations. The slight heterogeneity observed may arise from incomplete coating coverage or variable phosphate layer thickness, indicating that further optimization of the coating process could further enhance surface uniformity.

The schematic illustration (Figure 6c) outlines the in situ surface reconstruction mechanism via direct aqueous-phase coating. During ADP treatment, PO_4^{3-} ions react with residual Li^+ on the relithiated cathode surface to form Li_3PO_4, which subsequently crystallizes during annealing. The resulting conformal Li_3PO_4 coating serves a dual function. The coating suppresses Ni^{3+} overoxidation, thereby maintaining the Ni^{2+}/Ni^{3+} balance. The formation of Li_3PO_4 neutralizes residual lithium species, which otherwise contribute to surface degradation and impedance growth. These findings highlight that the benefits of phosphate surface reconstruction are strongly composition-dependent. While NCM622 with its moderate Ni content requires minimal passivation, NCMA significantly benefits from the Li_3PO_4 coating, which mitigates surface instability and improves the long-term cycling performance. This study demonstrates that surface engineering is essential for enhancing the durability of Ni-rich cathode materials, particularly in direct recycling applications.

CONCLUSIONS

This work introduces a scalable and compositionally versatile strategy for in situ surface reconstruction of Ni-rich cathodes through lithium residue regulation during cathode direct recycling. By utilizing ADP, the process simultaneously removes lithium residues and precipitates a conformal Li_3PO_4 layer that stabilizes the cathode−electrolyte interface. This dual-function coating suppresses surface overoxidation, mitigates phase transitions, and prevents transition metal dissolution without compromising Li^+ transport. Mechanistic and spectroscopic analyses confirm that the phosphate layer enhances redox uniformity and structural integrity, especially in high-Ni materials such as NCMA. Electrochemical testing shows that regenerated cathodes achieve high-capacity retention, improved rate capability, and reduced impedance—comparable to pristine benchmarks. The effectiveness of this method across both aged commercial materials (NCM622) and industrial scrap (NCMA) demonstrates its robustness and scalability. By integration of lithium residue regulation with in situ surface stabilization into a single, green processing step, this approach provides a sustainable and low-cost pathway for direct cathode regeneration. It supports the advancement of circular battery manufacturing and addresses critical challenges in resource-efficient energy storage solutions.

EXPERIMENTAL SECTION

Cathode Black Mass and Scrap Collection. Electrochemically aged $LiNi_{0.6}Co_{0.2}Mn_{0.2}O_2$ (NCM622) cathodes with significant capacity degradation were obtained from Canrd. Cells were fully discharged using resistors and manually disassembled inside a fume hood. Cathode sheets were carefully separated, cut into small pieces, and left exposed in the hood for 2 days to facilitate electrolyte evaporation. The electrode fragments were then vacuum-dried overnight at 80 °C for 12 h. The dried materials were pulverized by using a coffee grinder and sieved through a 63 μm mesh to obtain cathode black mass (CBM) powder. Separately, NCMA slurry waste ($LiNi_{0.866}Mn_{0.066}Co_{0.05}Al_{0.018}O_2$ mixed with the PVDF binder, Super P carbon, and NMP) was collected from the General Motors Wallace Battery Cell Innovation Center (WBCIC). Pristine NCM622 (P-NCM622, provided by Canrd, Guangdong) and pristine NCMA (provided by General Motor R&D, P-NCMA) were used as reference materials in all comparative analyses.

Cathode Active Material Regeneration. *Regeneration of NCM622.* A 100 g batch of CBM NCM622 was relithiated in 4 M LiOH solution at 220 °C via hydrothermal treatment. The resulting material was rinsed once with deionized water and designated as HT-NCM622. For surface reconstruction, the relithiated powder was divided into 5 g batches and treated with aqueous ammonium dihydrogen phosphate (ADP) solutions at various concentrations: 0.5, 1.0, 1.5, and 2.0 wt %. The mixtures were stirred at room temperature for 30 min to ensure homogeneous surface interaction. After drying under vacuum at 80 °C for 12 h, the ADP-treated powders were annealed at 850 °C for 4 h in pure oxygen with 5 mol % excess Li_2CO_3 to compensate for lithium loss. The resulting samples were labeled as "LPO-NCM622-0.5% ADP", "LPO-NCM622-1% ADP", "LPO-NCM622-1.5% ADP", and "LPO-NCM622-2% ADP", respectively. For comparison, a control sample designated as "DI-NCM622" was prepared without ADP treatment but was subjected to the same annealing process.

Regeneration of Scrap NCMA. To accommodate the binder-containing waste stream, a modified alkali-assisted relithiation process was applied as previously reported by our group.[19] A mixture of KOH pellets (20 wt %) and $LiOH{\cdot}H_2O$ (5 wt %) was stirred in ethanol for 2 h to prepare an alkali-alkoxide solution. A 100 g batch of scrap NCMA was added to 300 mL of this solution inside a 500 mL autoclave, followed by heating at 80 °C for 6 h with continuous stirring at 200 rpm. After cooling to room temperature without agitation, the regenerated CAM was separated by decanting the supernatant and rinsed with 50 mM LiOH solution. The filtered product was then treated with 1 wt % ADP solution and dried overnight at 60 °C. For final annealing, the powder was manually mixed with 5 mol % excess $LiOH{\cdot}H_2O$ and sintered at 750 °C for 6 h in a tube furnace under oxygen, with a ramping rate of 5 °C min^{-1}. The resulting sample was labeled as "LPO-NCMA".

Material Characterization. The elemental composition of the cathode powders was determined by inductively coupled plasma mass spectrometry (ICP−MS, Thermo Scientific iCAP RQ). Crystal structure and phase evolution were characterized by using X-ray diffraction (XRD, Bruker D2 Phaser, Cu Kα radiation, λ = 1.5406 Å). Surface chemical states were examined via X-ray photoelectron spectroscopy (XPS, PHI 5000 VersaProbe II, Al Kα, 1486.6 eV). Morphology and surface topography were observed by using scanning electron microscopy (SEM, FEI XL30). High-resolution transmission electron microscopy (HRTEM, Thermo Fisher Talos 200X) was used for particle-level imaging. STEM-EELS was performed in a high-angle annular dark-field (HAADF) mode with a Gatan Continuum imaging filter for elemental mapping. Thermogravimetric analysis (TGA) was conducted using a TA Instruments SDT650 under air, heating to 1000 °C at 10 °C min^{-1}. A 0.5 g portion of the cathode powder was dispersed in 30 mL of DI water into a centrifugal tube for the titration test. The centrifugal tubes were vigorously shaked, and the powder solution tubes were centrifuged at 5000 rpm for 10 min to extract surface lithium species. Then, 10 mL of the supernatant was titrated with 0.01 M HCl. The lithium content was calculated based on the volume of HCl consumed, and the surface lithium concentration of the sample was determined accordingly.

Soft X-ray absorption spectroscopy (XAS) measurements were carried out at the Stanford Synchrotron Radiation Lightsource (SSRL) bending magnet beamline 8−2 at a 55° incidence angle (magic angle) of X-ray incidence. The spectra were recorded using the 1000 lines/mm grating operated with 60 × 60 um slits for the Ni L-edge data (~0.35 eV resolution). The spot size at the interaction point was around 1×1 mm^2, and the total flux was in the order of 10^{10} photons/s for which beam damage was not noticeable even for extended exposure. The data were collected in both the total electron yield (TEY) and total fluorescence yield (TFY) modes using the drain current (amplified by a Keithley picoammeter) for TEY and a silicon diode (IRD AXUV-1000) for TFY. The incoming flux was recorded using a nickel grid with a Au-sputtered film (i0), collected in TEY, mounted upstream of the end station. Powder or electrode samples were loaded onto carbon tape and then stuck to an aluminum sample holder. Samples were sealed in an argon-filled glovebox and mounted on Al sample holders. Data were normalized using PyMCA software.[36] Transmission X-ray microscopy (TXM) was conducted at the National Synchrotron Light Source II of Brookhaven National Laboratory on Beamline FXI. The three-dimensional XANES map was acquired with a spatial resolution of 30 nm. Postprocessing was completed with TXM-Sandbox and Dragonfly 3D World.

Electrochemical Characterization. Electrochemical performance was evaluated in CR2032 coin-type half cells using regenerated, pristine, or spent cathodes. Electrode slurries were prepared by dispersing the active material, Super P (carbon black), and PVDF in the NMP solvent at a mass ratio of 8:1:1. The slurries were cast onto aluminum foil using a doctor blade, dried at 120 °C for 12 h under vacuum, and calendared before punching into 12 mm discs (~6 mg cm^{-2} loading).

Cells were assembled in an Ar-filled glovebox using lithium metal as the counter electrode, Celgard 2320 trilayer separator, and LP57 (1 M $LiPF_6$ in EC/EMC, 3:7) as the electrolyte. Cells were cycled on a Neware battery tester in the voltage range of 3.0−4.3 V. Four activation cycles were performed at C/10, followed by 100 cycles at C/3. Additional techniques such as the galvanostatic intermittent titration technique (GITT) and electrochemical impedance spectroscopy (EIS) was employed for kinetic and interfacial analyses. The GITT test was performed in the second cycle. Each current pulse lasted for 10 min at 0.1 C and was allowed to equilibrate for 180 min before starting the next pulse. The collected data were analyzed to determine the diffusion coefficient of the material. EIS was measured from 0.01 Hz to 100 kHz (Biologic potentiostat).

ASSOCIATED CONTENT

Supporting Information

The Supporting Information is available free of charge at https://pubs.acs.org/doi/10.1021/acsnano.5c13656.

Additional material characterizations, electrochemical performances, XRD analysis, and scale-up demonstration (PDF)

AUTHOR INFORMATION

Corresponding Authors

Linqin Mu − *Materials Science and Engineering, School for Engineering of Matter, Transport, and Energy, Arizona State University, Tempe, Arizona 85287, United States;* orcid.org/0000-0003-4421-4820; Email: linqinmu@asu.edu

Zheng Chen − *Aiiso Yufeng Li Family Department of Chemical and Nano Engineering, University of California, San Diego, La Jolla, California 92093, United States; Program of Materials Science and Engineering and Sustainable Power and Energy Center, University of California, San Diego, La Jolla, California 92093, United States;* orcid.org/0000-0002-9186-4298; Email: zhc199@ucsd.edu

Authors

Jiao Lin − *Aiiso Yufeng Li Family Department of Chemical and Nano Engineering, University of California, San Diego, La Jolla, California 92093, United States*

Varun Gupta − *Program of Materials Science and Engineering, University of California, San Diego, La Jolla, California 92093, United States;* orcid.org/0000-0002-4976-8593

Xiaolu Yu − *Program of Materials Science and Engineering, University of California, San Diego, La Jolla, California 92093, United States*

Yuwei Zhu − *Materials Science and Engineering, School for Engineering of Matter, Transport, and Energy, Arizona State University, Tempe, Arizona 85287, United States*

Dong Ju Lee − *Program of Materials Science and Engineering, University of California, San Diego, La Jolla, California 92093, United States;* orcid.org/0000-0002-8583-4957

Zishuo Zhao − *Materials Science and Engineering, School for Engineering of Matter, Transport, and Energy, Arizona State University, Tempe, Arizona 85287, United States*

Xianghui Xiao − *National Synchrotron Light Source II (NSLS-II), Brookhaven National Laboratory, Upton, New York 11973, United States;* orcid.org/0000-0002-7142-3452

Greta Feagure − *Aiiso Yufeng Li Family Department of Chemical and Nano Engineering, University of California, San Diego, La Jolla, California 92093, United States*

Feng Li − *Aiiso Yufeng Li Family Department of Chemical and Nano Engineering, University of California, San Diego, La Jolla, California 92093, United States;* orcid.org/0000-0003-0620-0639

Hongpeng Gao − *Program of Materials Science and Engineering, University of California, San Diego, La Jolla, California 92093, United States;* orcid.org/0000-0002-6640-4070

Dennis Nordlund − *Stanford Synchrotron Radiation Lightsource, SLAC National Accelerator Laboratory, Menlo Park, California 94025, United States*

Complete contact information is available at:
https://pubs.acs.org/10.1021/acsnano.5c13656

Notes

The authors declare no competing financial interest.

ACKNOWLEDGMENTS

Funding to support this work was provided by the US Department of Energy (Grant No. DE-EE0010399). Use of the beamline 10-1 at the Stanford Synchrotron Radiation Lightsource, SLAC National Accelerator Laboratory, is supported by the U.S. Department of Energy, Office of Science, Office of Basic Energy Sciences under Contract No. DE-AC02-76SF00515. This research used resources 18-ID, Full Field X-ray Imaging facility at the National Synchrotron Light Source II, a U.S. Department of Energy (DOE) Office of Science User Facility operated for the DOE Office of Science by Brookhaven National Laboratory under Contract No. DE-SC0012704.

REFERENCES

(1) Greim, P.; Solomon, A.; Breyer, C. Assessment of lithium criticality in the global energy transition and addressing policy gaps in transportation. *Nat. Commun.* **2020**, *11* (1), 4570.

(2) Mubarac, S.; Silva, M. N. T.; Silva, G. T. M.; Freitas, B.; Gonçalves, J. M.; Zanin, H. Super Ni-rich and Co-poor LiNixCoyMn1-x-yO2, LiNixCoyAl1-x-yO2, and LiNixCoyMnzAl1-x-y-zO2 ($x \geq 0.85$) based cathodes for lithium-ion batteries: A review on emerging trends, recent developments, and future perspectives. *J. Energy Storage* **2024**, *96*, No. 112612.

(3) Singh, J. P.; Devnani, H.; Sharma, A.; Lim, W. C.; Dhyani, A.; Chae, K. H.; Lee, S. Challenges and opportunities using Ni-rich layered oxide cathodes in Li-ion rechargeable batteries: the case of nickel cobalt manganese oxides. *Energy Adv.* **2024**, *3* (8), 1869−1893.

(4) Lin, J.; Li, W.; Chen, Z. Scaling Direct Recycling of Lithium-Ion Batteries toward Industrialization: Challenges and Opportunities. *ACS Energy Lett.* **2025**, *10* (2), 947−957.

(5) Azimi, G.; Chan, K. H. A review of contemporary and emerging recycling methods for lithium-ion batteries with a focus on NMC cathodes. *Resour. Conserv. Recycl.* **2024**, *209*, No. 107825.

(6) Fei, Z.; Xing, Y.; Dong, P.; Meng, Q.; Zhang, Y. Efficient direct regeneration of spent LiCoO2 cathode materials by oxidative hydrothermal solution. *Jom* **2023**, *75* (9), 3632−3642.

(7) Gao, H.; Yan, Q.; Xu, P.; Liu, H.; Li, M.; Liu, P.; Luo, J.; Chen, Z. Efficient Direct Recycling of Degraded LiMn2O4 Cathodes by One-Step Hydrothermal Relithiation. *ACS Appl. Mater. Interfaces* **2020**, *12* (46), 51546−51554.

(8) Yu, X.; Yu, S.; Yang, Z.; Gao, H.; Xu, P.; Cai, G.; Rose, S.; Brooks, C.; Liu, P.; Chen, Z. Achieving low-temperature hydrothermal relithiation by redox mediation for direct recycling of spent lithium-ion battery cathodes. *Energy Storage Mater.* **2022**, *51*, 54−62.

(9) Yang, Y.; Liu, Z.; Zhang, J.; Chen, Y.; Wang, C. Economical and low-carbon regeneration of spent LiFePO4 materials by hydrothermal relithiation. *J. Alloys Compd.* **2023**, *947*, No. 169660. Jiang, Z.; Xu, Z.; Li, L.; Wei, J.; Liu, Q.; Chen, Y.-C.; Xiao, T.; Lei, J.; Zhou, Y. Design Principles for Efficient Hydrothermal Relithiation of Spent Lithium Iron Phosphate. *ACS Appl. Mater. Interfaces* **2025**, *17* (3), 4875−4883.

(10) Gupta, V.; Yu, X.; Gao, H.; Brooks, C.; Li, W.; Chen, Z. Scalable direct recycling of cathode black mass from spent lithium-ion batteries. *Adv. Energy Mater.* **2023**, *13* (6), No. 2203093.

(11) Ryu, H.-H.; Lim, H.-W.; Lee, S. G.; Sun, Y.-K. Near-surface reconstruction in Ni-rich layered cathodes for high-performance lithium-ion batteries. *Nat. Energy* **2024**, *9* (1), 47−56.

(12) Liang, L.; Zhang, W.; Zhao, F.; Denis, D. K.; Zaman, F. U.; Hou, L.; Yuan, C. Surface/interface structure degradation of Ni-rich layered oxide cathodes toward lithium-ion batteries: fundamental mechanisms and remedying strategies. *Adv. Mater. Interface* **2020**, *7* (3), No. 1901749.

(13) Qu, X.; Huang, H.; Wan, T.; Hu, L.; Yu, Z.; Liu, Y.; Dou, A.; Zhou, Y.; Su, M.; Peng, X.; et al. An integrated surface coating strategy to enhance the electrochemical performance of nickel-rich layered cathodes. *Nano Energy* **2022**, *91*, No. 106665. Yu, H.; Cao, Y.; Chen, L.; Hu, Y.; Duan, X.; Dai, S.; Li, C.; Jiang, H. Surface enrichment and diffusion enabling gradient-doping and coating of Ni-rich cathode toward Li-ion batteries. *Nat. Commun.* **2021**, *12* (1), 4564.

(14) Yu, X.; Yu, S.; Lin, J.; Gupta, V.; Gao, H.; Li, W.; Appleberry, M.; Liu, P.; Chen, Z. Multifunctional Scavenger Boosts Cathode Interfacial Stability with Reduced Water Footprint for Direct Recycling of Spent Lithium-Ion Batteries. *Adv. Mater.* **2024**, *36* (41), No. 2408463. Su, Y.; Li, L.; Chen, L.; Wang, L.; Lu, Y.; Zhang, Q.; Bao, L.; Wu, F. Enhanced electrochemical performance of Ni-Rich cathode materials with an in situ-formed $LiBO_2/B_2O_3$ hybrid coating layer. *ACS Appl. Energy Mater.* **2022**, *5* (2), 2231−2241.

(15) Kim, J.; Hong, Y.; Ryu, K. S.; Kim, M. G.; Cho, J. Washing effect of a $LiNi_{0.83}Co_{0.15}Al_{0.02}O_2$ cathode in water. *Electrochem. Solid-State Lett.* **2006**, *9* (1), A19. Xiong, X.; Wang, Z.; Yue, P.; Guo, H.; Wu, F.; Wang, J.; Li, X. Washing effects on electrochemical performance and storage characteristics of $LiNi_{0.8}Co_{0.1}Mn_{0.1}O_2$ as cathode material for lithium-ion batteries. *J. Power Sources* **2013**, *222*, 318−325.

(16) Wu, Y.; Li, M.; Wahyudi, W.; Sheng, G.; Miao, X.; Anthopoulos, T. D.; Huang, K.-W.; Li, Y.; Lai, Z. Performance and stability improvement of layered NCM lithium-ion batteries at high voltage by a microporous Al_2O_3 sol−gel coating. *ACS omega* **2019**, *4* (9), 13972−13980. Riesgo-González, V.; Hall, D. S.; Märker, K.; Slaughter, J.; Wright, D. S.; Grey, C. P. Effect of Annealing on the Structure, Composition, and Electrochemistry of NMC811 Coated with Al_2O_3 Using an Alkoxide Precursor. *Chem. Mater.* **2022**, *34* (21), 9722−9735.

(17) Hu, J.; Wang, H.; Xiao, B.; Liu, P.; Huang, T.; Li, Y.; Ren, X.; Zhang, Q.; Liu, J.; Ouyang, X.; et al. Challenges and approaches of single-crystal Ni-rich layered cathodes in lithium batteries. *Natl. Sci. Rev.* **2023**, *10* (12), nwad252.

(18) Xu, P.; Guo, X.; Jiao, B.; Chen, J.; Zhang, M.; Liu, H.; Yu, X.; Appleberry, M.; Yang, Z.; Gao, H.; et al. Proton-exchange induced reactivity in layered oxides for lithium-ion batteries. *Nat. Commun.* **2024**, *15* (1), 9842.

(19) Gupta, V.; Potts, C.; Tran, D.; Gao, H.; Li, M.; Lin, J.; Chen, Z. Streamlining Ni-Rich LiNixMnyCozO2 Cathode Black Mass Purification for Direct Recycling and Upcycling through the Alkoxythermal Process. *Adv. Energy Mater.* **2025**, No. 2406083.

(20) Gan, Q.; Qin, N.; Wang, Z.; Li, Z.; Zhu, Y.; Li, Y.; Gu, S.; Yuan, H.; Luo, W.; Lu, L.; et al. Revealing Mechanism of Li3PO4 Coating Suppressed Surface Oxygen Release for Commercial Ni-Rich Layered Cathodes. *ACS Appl. Energy Mater.* **2020**, *3* (8), 7445−7455.

(21) Shin, D. J.; Joo, S. H.; Lee, D.; Shin, S. M. Precipitation of lithium phosphate from lithium solution by using sodium phosphate. *Can. J. Chem. Eng.* **2022**, *100* (12), 3760−3767.

(22) Yu, X.; Yu, S.; Lin, J.; Gupta, V.; Gao, H.; Li, W.; Appleberry, M.; Liu, P.; Chen, Z. Multifunctional Scavenger Boosts Cathode Interfacial Stability with Reduced Water Footprint for Direct Recycling of Spent Lithium-Ion Batteries. *Adv. Mater.* **2024**, *36* (41), No. 2408463.

(23) Liodakis, S. E.; Statheropoulos, M. K.; Tzamtzis, N. E.; Pappa, A. A.; Parissakis, G. K. The effect of salt and oxide-hydroxide additives on the pyrolysis of cellulose and Pinus halepensis pine needles. *Thermochim. Acta* **1996**, *278*, 99−108.

(24) Lee, Y.; Lee, J.; Lee, K. Y.; Mun, J.; Lee, J. K.; Choi, W. Facile formation of a Li3PO4 coating layer during the synthesis of a lithium-rich layered oxide for high-capacity lithium-ion batteries. *J. Power Sources* **2016**, *315*, 284−293.

(25) Wu, B.; Yi, R.; Xu, Y.; Gao, P.; Bi, Y.; Novák, L.; Liu, Z.; Hu, E.; Wang, N.; Rijssenbeek, J.; et al. Unusual Li2O sublimation promotes single-crystal growth and sintering. *Nat. Energy* **2025**, *10*, 605−615.

(26) Popović, L.; Manoun, B.; De Waal, D.; Nieuwoudt, M.; Comins, J. Raman spectroscopic study of phase transitions in Li3PO4. *J. Raman Spectrosc.* **2003**, *34* (1), 77−83.

(27) Shi, Y.; Zhang, M.; Meng, Y. S.; Chen, Z. Ambient-pressure relithiation of degraded LixNi0.5Co0.2Mn0.3O2 (0< x< 1) via eutectic solutions for direct regeneration of lithium-ion battery cathodes. *Adv. Energy Mater.* **2019**, *9* (20), No. 1900454.

(28) Cho, Y.; Oh, P.; Cho, J. A New Type of Protective Surface Layer for High-Capacity Ni-Based Cathode Materials: Nanoscaled Surface Pillaring Layer. *Nano Lett.* **2013**, *13* (3), 1145−1152.

(29) Tian, C.; Nordlund, D.; Xin, H. L.; Xu, Y.; Liu, Y.; Sokaras, D.; Lin, F.; Doeff, M. M. Depth-dependent redox behavior of LiNi0.6Mn0.2Co0.2O2. *J. Electrochem. Soc.* **2018**, *165* (3), A696−A704.

(30) de Groot, F. M.; Fuggle, J.; Thole, B.; Sawatzky, G. 2p x-ray absorption of 3d transition-metal compounds: An atomic multiplet description including the crystal field. *Phys. Rev. B* **1990**, *42* (9), 5459.

(31) Lin, F.; Markus, I. M.; Nordlund, D.; Weng, T.-C.; Asta, M. D.; Xin, H. L.; Doeff, M. M. Surface reconstruction and chemical evolution of stoichiometric layered cathode materials for lithium-ion batteries. *Nat. Commun.* **2014**, *5* (1), 3529.

(32) Xie, Y.; Li, J.; Li, M.; Cai, J.; Huang, X.; Nguyen, H.; Yu, L.; Huo, D.; Yang, Z.; Karami, N. Modifying Surface Chemistry to Enhance the Electrochemical Stability of Nickel-Rich Cathode Materials. *Adv. Funct. Mater.* **2024**, *34* (14), No. 2311551. Gao, S.; Wang, L.; Zhou, C.; Guo, C.; Zhang, J.; Li, W. In-situ construction protective layer and phosphate doping synergistically improve the long-term cycle stability of $LiNi_{0.6}Co_{0.1}Mn_{0.3}O_2$. *Chem. Eng. J.* **2021**, *426*, No. 131359.

(33) Tröger, L.; Arvanitis, D.; Baberschke, K.; Michaelis, H.; Grimm, U.; Zschech, E. Full correction of the self-absorption in soft-fluorescence extended x-ray-absorption fine structure. *Phys. Rev. B* **1992**, *46* (6), 3283−3289. Eisebitt, S.; Böske, T.; Rubensson, J. E.; Eberhardt, W. Determination of absorption coefficients for concentrated samples by fluorescence detection. *Phys. Rev. B* **1993**, *47* (21), 14103−14109.

(34) Ma, L. A.; Massel, F.; Naylor, A. J.; Duda, L.-C.; Younesi, R. Understanding charge compensation mechanisms in Na0.56Mg0.04-Ni0.19Mn0.70O2. *Commun. Chem.* **2019**, *2* (1), 125.

(35) Liang, C.; Zhang, W.; Wei, Z.; Wang, Z.; Wang, Q.; Sun, J. Transition-metal redox evolution and its effect on thermal stability of LiNixCoyMnzO2 based on synchrotron soft X-ray absorption spectroscopy. *J. Energy Chem.* **2021**, *59*, 446−454.

(36) Solé, V. A.; Papillon, E.; Cotte, M.; Walter, P.; Susini, J. A multiplatform code for the analysis of energy-dispersive X-ray fluorescence spectra. *Spectrochim Acta Part B At Spectrosc.* **2007**, *62* (1), 63−68.